Journal of Applied Fluid Mechanics, Vol. 10, No. 1, pp. 353-368, 2017.
Available online at www.jafmonline.net, ISSN 1735-3572, EISSN 1735-3645.
DOI: 10.18869/acadpub.jafm.73.238.26185

Asymmetric Water Entry of Twin Wedges with Different Deadrises, Heel Angles, and Wedge Separations using Finite Element Based Finite Volume Method and VOF

R. Shademani and P. Ghadimi†

Department of Marine Technology, Amirkabir University of Technology, Tehran, 14717, Iran

†*Corresponding Author Email: pghadimi@aut.ac.ir*

(Received February 6, 2016; accepted July 13, 2016)

ABSTRACT

Asymmetric water entry of twin wedges is investigated for deadrise angles of 30 and 50 degrees, and heel angles of 5, 10, 15, and 20 degrees as well as wedge separation ratios of 1 and 2. Finite Element based Finite Volume method (FEM-FVM) is used in conjunction with Volume of Fluid (VOF) scheme for the targeted analyses. Free surface evolution and impact forces versus time are determined and comparisons of the maximum force of the wedges against each other are presented for all the considered cases. It is demonstrated that the impact force on the second wedge is always greater than the first one by a minimum of 6% and maximum of 146% which is a very significant increase in the impact force and may cause high accelerations and damage to the structure. It is also observed that the mentioned effects increase with decreasing deadrise angle and increasing heel angle.

Keywords: Catamaran; Asymmetric water entry; Twin wedges; FEM-FVM; Heel angle.

NOMENCLATURE

A	closed surface bounding
d	Twin wedge separation
$\vec{d}$	vector between the cell centers
dA	Surface element
g_i	gravitational acceleration
N	shape function
p	static pressure
u	velocity in x direction
s	source term
W	half width of the wedge
V	velocity in y direction
V_P	cell volume
$\vec{V}$	velocity vector
α	volume fraction
ρ_l	liquid density(water)
ΔS_U	distance of the integration point from the upwind point
ρ_g	gas density(air)
φ	parameter value at integral point like u and v
$\tilde{\alpha}_C^{t+\delta t}$	normalized volume fraction at a cell (sub-elements)
Φ_i	nodal value of any arbitrary φ
$\tilde{\alpha}_C^t$	value of $\tilde{\alpha}_P$ from the previous time step
$\tilde{\alpha}_f$	normalized volume fraction at face point
$\tilde{\Omega}_i$	value of sub-volumes of each element
$\tilde{\alpha}_D$	normalized volume fraction at Donor point
$\tilde{\alpha}_f^*$	approximation of time-averaged normalized volume fraction at face value.
α_f^*	time-average volume fraction at face point
μ_g	gas dynamic viscosity
Ω	control volume
μ_l	liquid dynamic viscosity
o	center of control volume
δt	time interval
Q_f	volumetric flux through the face

1. INTRODUCTION

The first study on the water entry was carried out by Von Karman (1929) and Wagner (1932), who have investigated this problem on wedges and circular cylinders. This issue which involves the evaluation of impact forces and spray formation due to the entry of wedges into water is significantly important in many hydrodynamic and structural problems in the marine industries. The studies of Von Karman and Wagner were followed by Zhao *et al.* (1993, 1996, 1998) and Faltinsen (2002, 2004) who presented an in depth analysis on the subject in 1990s. However, despite the age of the physical phenomenon which dates back to nearly a century, many aspects of the problem are still uncharted. Study of this problem, which is a critical need for implementation of the 2D+t theory (Ghadimi *et al.* (2015)), and many structural problems relating to hull slamming of planing hulls, is increasingly used in the analysis of different geometries in maritime industries.

The growth of the catamarans and twin hull vessels requires a better knowledge about the symmetric and asymmetric water entry of these structures, the latter being the focus of the present paper. However, before addressing this issue, literature related to different aspects of the problem is briefly reviewed.

Wedge water entry has been numerically investigated by many researchers. Yang and Qiu (2012), Wu (2012) and Luo *et al.* (2011) can be mentioned among others who investigated the water entry forces and free surface, numerically. Also, Shademani and Ghadimi (2016) numerically investigated the secondary impact of wedges at extreme angles. Boundary element method was also used by Zhao and faltinsen (1993), Battistin and Iafrati (2004), Sun *et al.* (2011), Wang and Wei (2012), Yousefnezhad and Zeraatgar (2014) and Gao *et al.* (2011). In a different approach, the Shwartz-Christoffel conformal mapping was used by Ghadimi *et al.* (2011) as an analytical solution to the problem. Moreover, Shah *et al.* (2015) analyzed the impact of rigid wedges on water in 2D fluid flow through experimental and SPH methods.

To investigate the effects of the wedge flexibility on the water entry, Panciroli (2012, 2013) and Piro and Maki (2013) numerically studied the water entry of flexible wedges.

As mentioned before, wedges are not the only shapes studied in the water entry problems. Circular cylinders have been investigated by Greenhow (1988), Zhu (2006), and Ghadimi *et al.* (2012), while arbitrary sections have been studied by Ghadimi *et al.* (2013, 2014).

Meanwhile, the smoothed particle hydrodynamics method (SPH) has also been used to analyze the wedge water entry problem by Farsi and Ghadimi (2013, 2014a, and 2014b). Yamada *et al.* (2012), Luo *et al.* (2012), Mutsuda and Doi (2009) Khabakhpasheva and korobkin (2012), and Mo *et al.* (2011), are among other researchers who have investigated this problem.

In the field of catamaran water entry, the effect of hull separation on impact forces and spray formation has been investigated by He *et al.* (2011) for a specific catamaran with a single deadrise and with no heel angle. Also the catamaran water entry has been investigated by Farsi and Ghadimi (2014a), again for a single catamaran section.

The present paper focuses on the numerical solution of the asymmetric water entry of twin wedges in different heel angles and with different deadrise angles. The effects of the distance between the wedges on the free surface and impact forces of the wedges are investigated, separately. In order to conduct the calculations, the Finite Volume based Finite Element is used as numerical method, while Volume of Fluid is utilized for the free surface modeling. In the following section, the governing equations and the numerical method are discussed, followed by validation of the code and the results and discussion.

2. GOVERNING EQUATIONS AND NUMERICAL METHOD

Navier Stokes equations for transient, incompressible, and laminar flow with negligible dissipation effects are calculated for two-phase flow using FEM-FVM method coupled with the VOF method. Two-dimensional incompressible form of the conservation of mass is as follows:

$$\int_A \rho \vec{V}.\vec{dA} = 0 \tag{1}$$

The conservation of momentum is:

$$\underbrace{\frac{\partial}{\partial t}\int_\Omega \rho\varphi d\Omega}_{Transient} + \underbrace{\int_A \rho u\varphi dA_x + \int_A \rho v\varphi dA_y}_{Convection} = \underbrace{-\int_A (\Gamma\frac{\partial\varphi}{\partial x}dA_x + \Gamma\frac{\partial\varphi}{\partial y}dA_y)}_{Diffusion} + \underbrace{\int_\Omega \mathbf{S}d\Omega}_{Source} \tag{2}$$

where φ, Γ and $\mathbf{S}$ are expressed as follows:

in x-Momentum equation:

$$\varphi = u, \qquad \Gamma = \mu, \qquad \mathbf{S} = -\frac{\partial P}{\partial x} + \rho g_x$$

in y-Momentum equation: (3)

$$\varphi = v, \qquad \Gamma = \mu, \qquad \mathbf{S} = -\frac{\partial P}{\partial y} + \rho g_y$$

Here, g_x and g_y are the gravitational accelerations in x and y direction, respectively, but g_x is equal to zero.

In the present work, the momentum equations are implemented in control volumes which result in four terms presented in Eq. (2).

Matrix coefficients related to this equation are as follows:

$$[cd]_{3\times3} : \text{Diffusion} \tag{4}$$

$[ct]_{3\times3}$: Transition

$[cc][cp]_{3\times3}$: Convection

$[dp]_{3\times3}$: Source

$[dd]_{3\times1}$: Constant

Eqs. (2) and (4) can be rewritten in matrix form as

$$[cd]\{\varphi\}+[ct]\{\varphi\}+[cc]\{\varphi\} + [cp]\{p\}+[dp]\{p\}+\{dd\}=0 \quad (5)$$

Discretization of Eq. (2) is described in the following sections.

2.1 Transient Term

Transient term is a volumetric parameter that is integrated over the cell volume. The integral version is transformed into differential form in time domain as

$$\frac{\partial}{\partial t}\int_{\Omega}\rho\varphi d\Omega=\left(\frac{\partial\rho\Phi}{\partial t}\right)_i\tilde{\Omega}_i=\frac{\rho\Phi_i-\rho\Phi_i^O}{\Delta t}\tilde{\Omega}_i \quad (6)$$

Therefore, Eq. (6) can be written in matrix form as

$$[ct]=\frac{\rho}{\Delta t}\begin{bmatrix}\tilde{\Omega}_1 & 0 & 0\\ 0 & \tilde{\Omega}_2 & 0\\ 0 & 0 & \tilde{\Omega}_3\end{bmatrix},\ [dd]=\frac{\rho}{\Delta t}\begin{bmatrix}\Phi_1^O\tilde{\Omega}_1\\ \Phi_2^O\tilde{\Omega}_2\\ \Phi_3^O\tilde{\Omega}_3\end{bmatrix} \quad (7)$$

Matrices [*ct*] and [*dd*] are updated and substituted in the assembly matrix.

2.2. Source Term

In Eq. (2), the source term is the summation of pressure gradient and gravity effects and can be presented as for *x*-momentum and *y*-momentum as in

$$\int_{\Omega}\mathbf{S}d\Omega=\int_{\Omega}(-\frac{\partial p}{\partial x}+\rho g_x)d\Omega= -\int_A pdA_x+\int_{\Omega}\rho g_x d\Omega=-\sum_{k=1}^{3}N_kP_kdA_x+\rho g_x\sum_{k=1}^{3}\tilde{\Omega}_k \quad (8a)$$

$$\int_{\Omega}\mathbf{S}d\Omega=\int_{\Omega}(-\frac{\partial p}{\partial y}+\rho g_y)d\Omega=-\int_A pdA_y+\int_{\Omega}\rho g_y d\Omega= -\sum_{k=1}^{3}N_kP_kdA_y+\rho g_y\sum_{k=1}^{3}\tilde{\Omega}_k \quad (8b)$$

Bilinear interpolation method is applied for discretization of the pressure term. Here, P_k indicates the nodal pressure values at each of the three integration points and the shape function N_k indicates the contribution of them.

The source term is a volumetric parameter. Matrices [*dp*] and [*dd*] are updated at this stage.

2.3. Convection Term

Discretization of the convection term on the control line *j,k* accomplished as in

$$\int_{A_{j,k}}\rho(\vec{V}.\vec{dA})\varphi=(\rho\vec{V}.\vec{dA})_{j,k}\varphi_{j,k} \quad (9)$$

For discretizing φ, using upwind difference scheme (UDS) in two directions of x and y causes false diffusion. In such a case, the application of UDS is assumed to occur in the direction of *x* and *y* at the integration point j shown in Fig. 1. However, in order to eliminate the false diffusion problem, the upwind scheme (US) for should be applied in the flow direction at integration point j which is illustrated in Fig. 1. Same would apply to integration point k at which the upwind scheme would also be applied in the designated "flow direction".

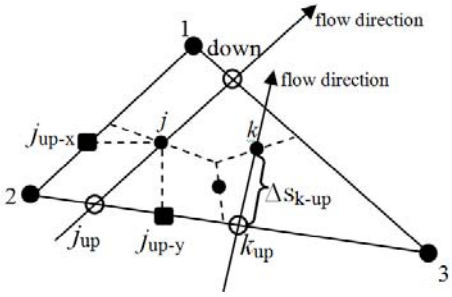

Fig. 1. Flow direction in integration points.

Moreover, the method proposed by Karimian and Schneider (1994) is utilized which given as

$$(\rho\vec{V}.\vec{dA})_{j,k}\varphi_{j,k}=(\rho\vec{\hat{V}}.\vec{dA})_{j,k}\varphi_{j,k} \quad (10)$$

where $\vec{\hat{V}}$ is the velocity vector defined by Karimian and Schneider's scheme (1994) to prevent the checkerboard problem. The components of the vector are calculated using Eqs. (11) and (12).

$$\hat{u}_j=U_{L-S}-\frac{\Delta S_U}{\rho\bar{\bar{V}}}\left\{\begin{matrix}-\rho\left(u\frac{\partial v}{\partial y}-v\frac{\partial u}{\partial y}\right)\\ +\rho\frac{\partial u}{\partial t}+\frac{\partial P}{\partial x}-\mu\overline{\nabla^2 u}\end{matrix}\right\} \quad (11)$$

$$\hat{v}_j=V_{L-S}-\frac{\Delta S_U}{\rho\bar{\bar{V}}}\left\{\begin{matrix}-\rho\left(v\frac{\partial u}{\partial x}-u\frac{\partial v}{\partial x}\right)\\ +\rho\frac{\partial v}{\partial t}+\frac{\partial P}{\partial y}-\mu\overline{\nabla^2 v}\end{matrix}\right\} \quad (12)$$

where ΔS_U is illustrated in Fig. 1. $U_{L\text{-}S}$ and $V_{L\text{-}S}$ are calculated using a bilinear interpolation on the velocity. Also, the bar sign on any variable indicates the value from the previous time step. Accordingly, $\bar{\bar{V}}$ is the velocity from the previous time step. The final form of the continuity equation is presented as

$$(\rho\hat{u}dA_x)_j+(\rho\hat{u}dA_x)_k+(\rho\hat{v}dA_y)_j+(\rho\hat{v}dA_y)_k=0 \quad (13)$$

Also, in Eq. (10), φ_j is calculated using the relation

$$\varphi_j=\varphi_{upj}+\frac{\partial\varphi}{\partial A}\Delta s \quad (14)$$

where φ_{upj} is the upwind velocity at integration

point *j*, as shown in Fig. 1, and $(\partial\varphi/\partial A)\Delta s$ is a linear estimation of the variation of φ from the upwind point to the integration point

2.4. Diffusion Term

The diffusion term is modeled as

$$-\int_{A_{j,k}} \Gamma(\overrightarrow{\nabla\phi}.\overrightarrow{dA}) = -\Gamma\overrightarrow{\nabla\phi}.\overrightarrow{dA}\Big|_{j,k} = -\left(\Gamma\frac{\partial\phi}{\partial x}dA_x + \Gamma\frac{\partial\phi}{\partial y}dA_y\right)\Big|_{j,k} \tag{15}$$

Calculations of $\partial\varphi/\partial x$ and $\partial\varphi/\partial y$ are performed using shape functions. These terms are determined by

$$\frac{\partial\varphi}{\partial x} = \sum_{i=1}^{3}\frac{\partial N_i}{\partial x}\Phi_i \tag{16a}$$

$$\frac{\partial\varphi}{\partial y} = \sum_{i=1}^{3}\frac{\partial N_i}{\partial y}\Phi_i \tag{16b}$$

[*cd*] is a 3×3 matrix and each row belongs to a sub-volume, as shown in Fig. 3.

$$\left[cd_{j,i}\right] = \frac{\partial N}{\partial x}\Big|_{j,i}\times dA_x\Big|_{j,j} + \frac{\partial N}{\partial x}\Big|_{k,i}\times dA_x\Big|_{j,k} + \frac{\partial N}{\partial y}\Big|_{j,i}\times dA_y\Big|_{j,j} + \frac{\partial N}{\partial y}\Big|_{k,i}\times dA_y\Big|_{j,k} \tag{17}$$

In Eq. (17), *j* is the sub-volume indicator and *k* is the integration points of each sub-volume and *i* any of the three nodes that embody each element.

2.5. VOF Modeling

Volume of Fluid (VOF) method is based on the conservation of volume fraction (α) with respect to time and space which is formulated as

$$\frac{\partial\alpha}{\partial t} + \frac{\partial(u\alpha)}{\partial x} + \frac{\partial(v\alpha)}{\partial y} = 0 \tag{18}$$

In the VOF method, volume fraction (α) is a scalar parameter which represents the fraction of a cell filled with one fluid, while assuming $1-\alpha$ represents the volume fraction of the second fluid. When $\alpha = 1$, the cell is filled by the first fluid and the density/viscosity of the first fluid is used. On the other hand, when $\alpha = 0$, the cell is filled by the second fluid and the properties of the second fluid are implemented. When $0 < \alpha < 1$, the cell contains a portion of both fluids and equivalent properties should be used. To consider a general formulation of these three cases using the volume fraction approach, the equivalent density and viscosity of the cells are expressed as follows:

$$\rho_{eq} = \alpha\rho_l + (1-\alpha)\rho_g$$
$$\mu_{eq} = \alpha\mu_l + (1-\alpha)\mu_g \tag{19}$$

Physical properties are estimated by a linear mixture assumption. In finite volume method, α is calculated on each cell center and is used in governing differential equation of conservation of volume fraction function. In finite element based finite volume, nodal points of elements are utilized for applying this conservation equation. Based on these properties, the VOF method in

$$\frac{\partial}{\partial t}(\rho) + \nabla.(\rho V) = 0 \tag{20}$$

is transformed to

‼ EMBED Equation.3

$$\frac{\partial\alpha}{\partial t} + V.\nabla\alpha + \alpha\nabla.V = -\frac{\rho_g\nabla.V}{(\rho_L - \rho_g)} \tag{21}$$

For incompressible two phase flow without any phase change, ∇.V is zero, and the Eq. (21) reduces to Eq. (18). The finite-volume discretization of Eq. (18) leads to

$$\alpha_C^{t+\delta t} = \alpha_C^t + \frac{\delta t}{V_C}\sum_{f=1}^{n}\alpha_f^* Q_f \tag{22}$$

Cell-centered values of α are used to interpolate the face values α_f^*. In finite element based finite volume method, integration point is used as a cell center and donor-acceptor flux approximation is utilized for simulation of α. Concept of donor-acceptor method has been described by Ubbink and Issa (1999). In the present study, this method (formulated in Eq. (22)) has been altered and used for unstructured mesh and finite element method. The applied method uses CICSAM scheme (Ubbink and Issa (1999)) in Eq. (22) based on the normalized variable diagram (NVD) which is found by the normalized values of volume fraction calculated based on the general relation

$$\tilde{\alpha} = \frac{\alpha - \alpha_U}{\alpha_A - \alpha_U} \tag{23}$$

This equation can be used to normalize the volume fraction at any point like the integral point or a point which is located between two main points on the element boundary. According to Eq. (23), normalized volume fraction ($\tilde{\alpha}$) is presented as a function of upwind (α_U) and acceptor (α_A) nodal values. Equation (22) is solved by an iterative method based on the normalized parameters and volume fraction at nodal points is calculated using Eq. (23) (i.e. $\alpha = \alpha_U + \tilde{\alpha}(\alpha_A - \alpha_U)$). To calculate the normalized values at donor ($\tilde{\alpha}_D$) and acceptor ($\tilde{\alpha}_f$) points, Eq. (23) is utilized as follows:

$$\tilde{\alpha}_D = \frac{\alpha_D - \alpha_U}{\alpha_A - \alpha_U} = 1 + \frac{\alpha_D - \alpha_A}{2(\nabla\alpha)_D.\vec{d}} \tag{24}$$

$$\tilde{\alpha}_f = \frac{\alpha_f - \alpha_U}{\alpha_A - \alpha_U} = 1 + \frac{\alpha_f - \alpha_A}{2(\nabla\alpha)_D.\vec{d}} \tag{25}$$

where subscripts *U*, *D* and *A* indicate the upwind, donor and acceptor cells, respectively. Also, $\vec{d}$ is the vector between the cell centers of the donor and acceptor cells as presented in Fig. 2 and

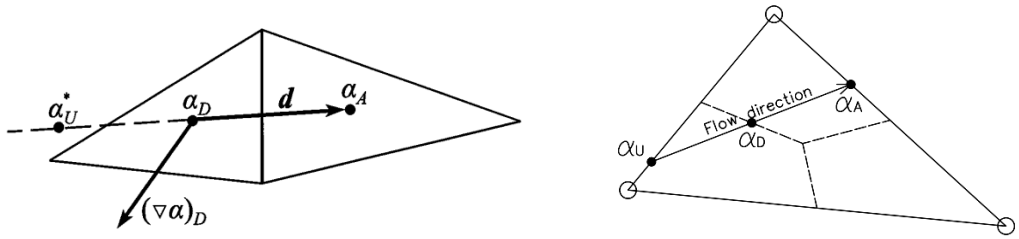

(a) **(b)**

Fig. 2. a) Prediction of the upwind value for an arbitrary cell arrangement (presented by Ubbink and Issa, (1999)), and b) New modification of donor-acceptor scheme.

$\alpha_U = \alpha_A - 2(\bar{\nabla}\alpha)_D.\vec{d}$.

Equation (22) is rewritten in normalized value fashion as

$$\tilde{\alpha}_C^{t+\delta t} = \tilde{\alpha}_C^t + \frac{\delta t}{V_C}\sum_{f=1}^{n}\tilde{\alpha}_f^* Q_f \tag{26}$$

Normalized values are calculated based on Eqs. (24) and (25).

In the current study, donor-acceptor scheme is used for each sub-element. Integral points are assumed as donor cells or points (see Fig. 2b), and α is predicted based on the shape functions. Shape functions are utilized for calculating α_U based on these values at the nodal points. Three nodal values are saved for each element. Accordingly, α_U can be predicted in two ways: 1) through using shape functions in local coordinates and 2) by linear interpolation of two neighboring nodes. The second method is adopted for the current study. New values of U are updated in every time step at the integral points and flow direction is set. Subsequently, α_U and α_A are calculated and the donor-acceptor scheme is reapplied.

When using VOF method, Eq. (19) is implemented in place of fluid properties in the Navier-Stokes equations. This way, although the Navier-Stokes equations are solved simultaneously for both fluids as one, the free surface can be extracted using the volume fraction. Based on the initial conditions, values of α are applied on the nodal points. Subsequently, these parameters are interpolated by shape functions and estimated on the integral points. In each time step, flow pattern is generated and velocity vectors are determined at the integral points. Consequently, donor and acceptor nodes are set and Eq. (22) is solved in each sub-element using normalized values. Then, new values of α are calculated based on the normalized values of α from the previous time step obtained from Eq. (23).

At this stage, new volume fractions of the cells located on the boundary of the two-phase flow are updated and the free surface is determined for this time step. The new values of α are calculated at integral points and are extended to the element points by shape functions. Each element has a volume fraction value that can be calculated based on three nodal points. In the visualizations, the free surface represents α=0.5.

The applied numerical method is briefly explained in the next section.

2.6. Finite-Element Concepts

As pointed out earlier, triangular grids are used in the current study, as shown in Fig. 2. General form of a typical mesh is displayed in Fig. 3. The sub-volumes of element (Ω), as noted in equation (6), are shown in Fig.3. For reducing the computing time, the origin has been moved to each integration point (ip) and the coordinate system (x-y) has been rotated (to s-t coordinate system) in order to place x coordinate in the direction of the velocity vector at that integration point. As a result, less computational power is required for calculations related to shape functions or geometrical characteristics of elements.

Shape functions are defined on each node of the elements as $\phi = \sum_{i=1}^{Node} N_i\phi_i$, where N_i is the shape function at node *i*, while φi is the value of φ at that node. The method utilized in this paper is based on the fully coupled Rhie and Chow (1983) algorithm applied on a collocated triangular grid system for a 2D fluid flow. The shape functions for the triangular elements are as follows:

$$\begin{aligned}
N_1 &= (\frac{y_2 - y_1}{DET})x + (\frac{x_3 - x_2}{DET})y + (\frac{x_2y_3 - x_3y_2}{DET}) \\
N_2 &= (\frac{y_3 - y_1}{DET})x + (\frac{x_1 - x_3}{DET})y + (\frac{x_3y_1 - x_1y_3}{DET}) \\
N_3 &= (\frac{y_1 - y_2}{DET})x + (\frac{x_2 - x_1}{DET})y + (\frac{x_1y_2 - x_2y_1}{DET})
\end{aligned} \tag{27}$$

$$DET = \begin{pmatrix} x_1y_2 + x_2y_3 + x_3y_1 \\ -y_1x_2 - y_2x_3 - y_3x_1 \end{pmatrix}$$

The involved terms in these equations are discretized on control lines between each two nodes.

The overall algorithm of the code is illustrated in Fig. 4. As observed in Fig. 4, Navier Stokes equations are solved, first. Subsequently, the VOF equations are solved using the velocities resulting from the Navier Stokes equations.

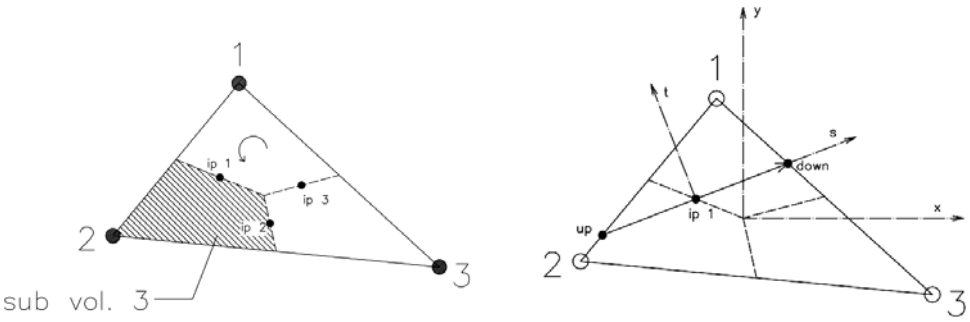

Fig. 3. A typical triangular element and calculation of up and down points of the velocity vector through the integration points.

Afterward, using the obtained volume fraction, the new density and viscosity in each element are calculated and fed into the Navier Stokes equations for the next time step.

A computer code is developed based on this algorithm for solving the two phase flow problem of the wedge water entry. In the next section, the developed code is validated using previously published water entry data.

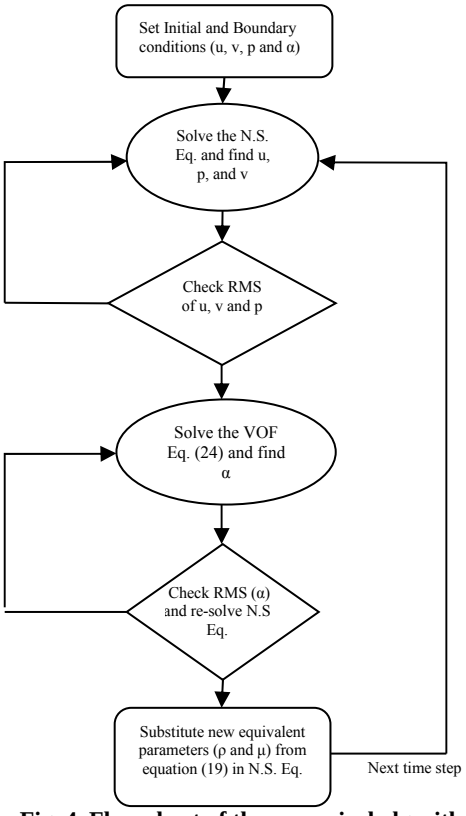

Fig. 4. Flow chart of the numerical algorithm.

3. VALIDATION

Experimental results of Tveitnes *et al.* (2008) are used to validate the developed code. Boundary conditions and the setup of the validation case are presented in Fig. 5.

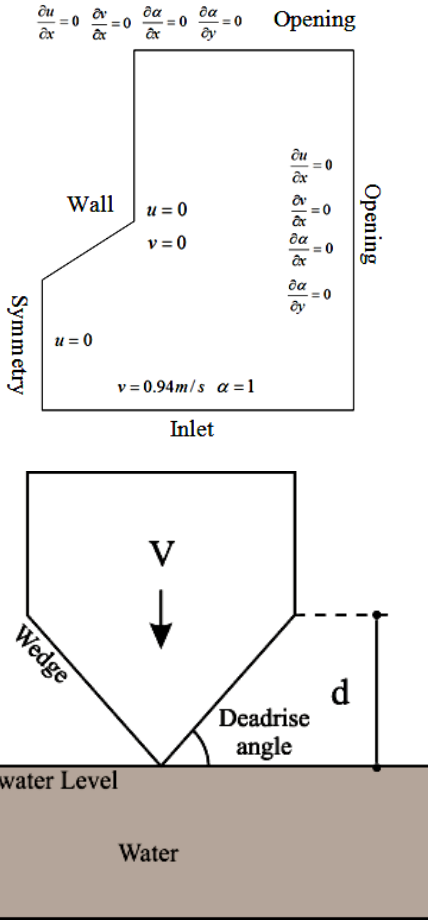

Fig. 5. Definition of the boundary conditions and parameters in the validation test.

The single wedge water entry is analyzed for two wedges with deadrises 10 and 15 degrees. The wedges are 0.6 m wide with an entry speed of 0.94 m/s. Comparison of the obtained forces against experimental results are presented in Fig. 6, where Z is the immersion depth of the apex.

It is evident that the code is valid for water entry forces on wedges with a mean error of 5.36% and maximum error of 10.5% for 10 degrees deadrise, and 7.48% mean error and 13.4% maximum for 15 degrees deadrise angle. Also, the free surface

results are compared with experimental data [34] in Fig. 7 to validate the free surface modeling. As observed in this figure, the free surface is also well modeled, keeping in mind that the free surface modeling errors are cumulative. In the next section, the results and discussions are presented.

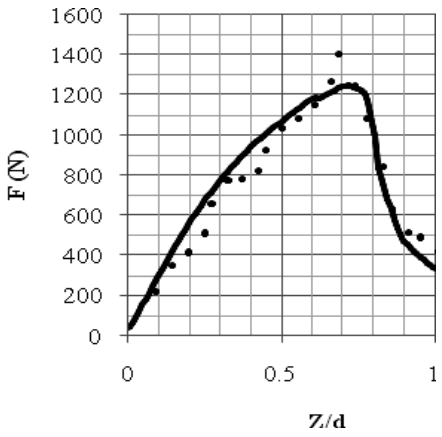

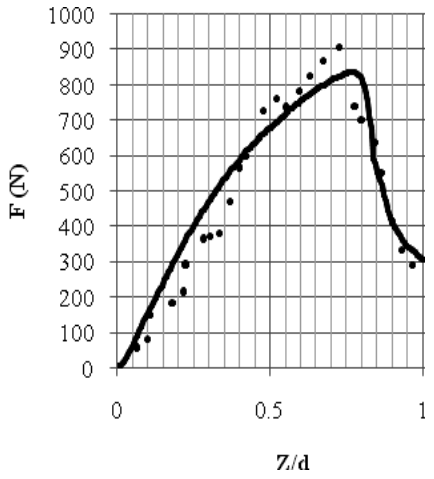

Fig. 6. Water entry force (F) Vs normalized Apex depth (Z/d): Comparison of numerical results (-) versus experimental data (.) [34] for deadrise angles of a) 10 degrees and b) 15 degrees.

4. RESULTS AND DISCUSSION

As pointed out earlier, water entry of twin wedges with different separations (d), deadrise angles, and heel angles is investigated, in the present study. The definition of the problem is illustrated in Fig. 8.

As indicated in Fig. 8, W is the half width of the wedge, which is hereby constant and equal to 1m. Values of the parameters under investigation are presented in Table 1.

Combination of the designated parameters in Table 1 yields to 16 cases which are analyzed and discussed in the present section. To this end, a two phase domain is considered with two similar wedges and the water which enters the domain from the bottom at the speed of the water entry (2 m/s). The boundary conditions of the domain are illustrated in Fig. 9.

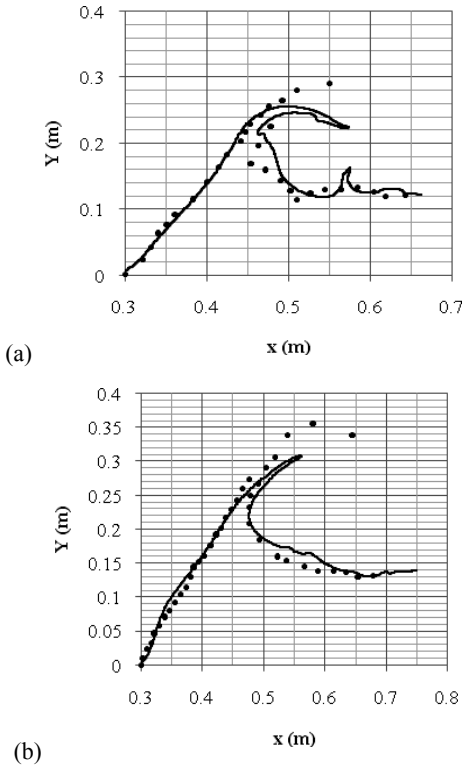

Fig. 7. Free Surface: Comparison of numerical results (-) versus experimental data (.) [34] for a) 10 degrees (at 0.1705s after entry) and b) 15 degrees deadrise angle (at 0.2265s after entry).

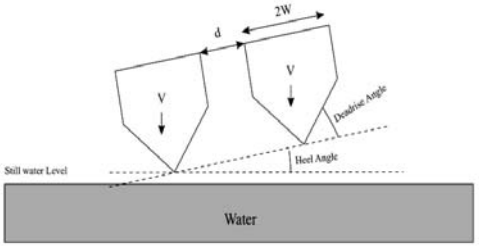

Fig. 8. Definition of the parameters.

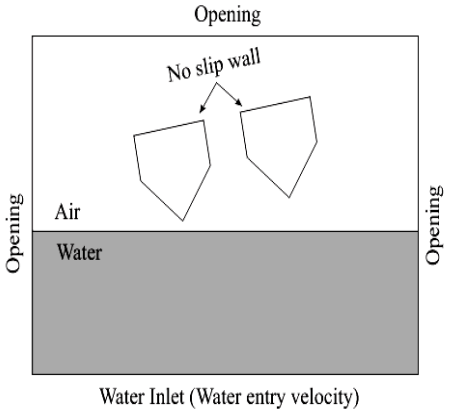

Fig. 9. Domain and boundary conditions.

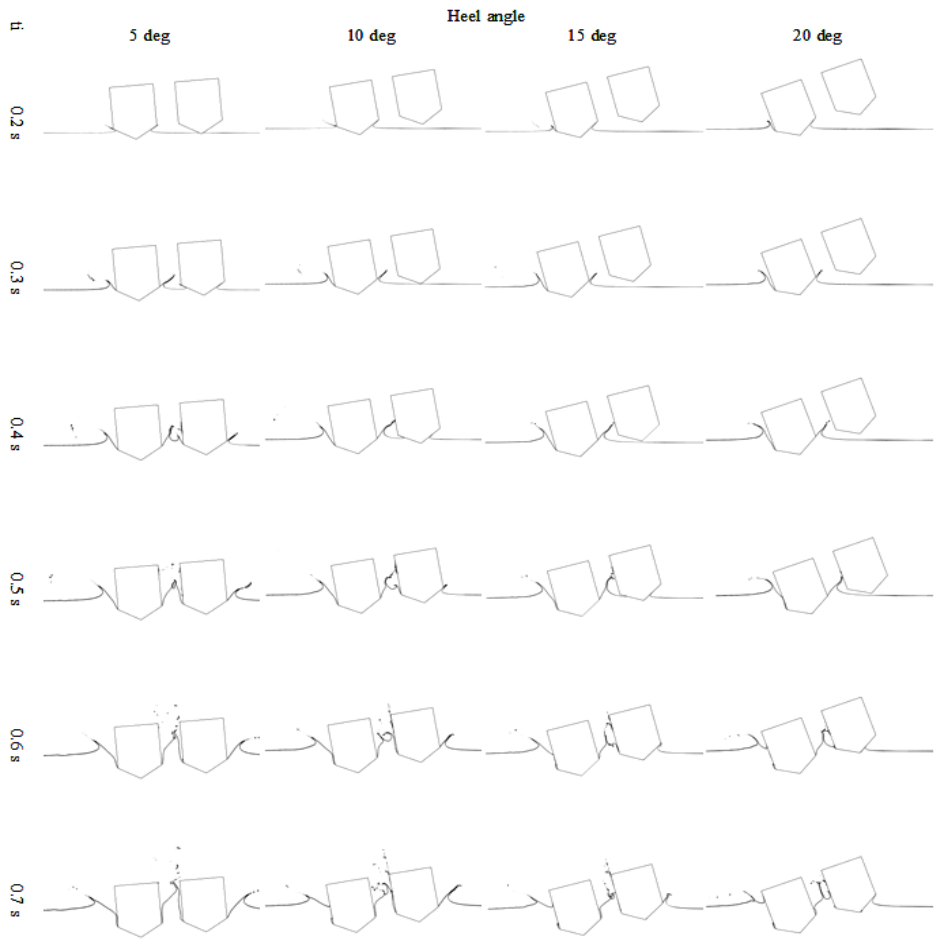

Fig. 10. Free surface evolution at different heel angles, deadrise = 30 deg., d/W = 1.

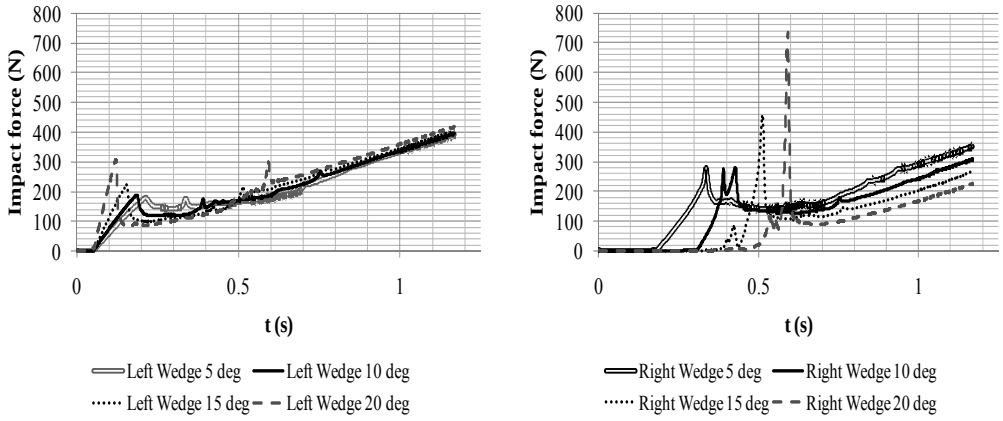

Fig. 11. Impact force Vs time at different heel angles for the left and right wedges, deadrise = 30 deg., d/W = 1.

Table 1 Value of parameters under investigation

Heel	5	10	15	20
Deadrise	30	50		
d/W	1	2		

Based on the computational analysis of the defined cases, the results are presented in the form of free surface evolution, left (first) wedge impact force, right (second) wedge impact force, the maximum impact force and time of the occurrence for both wedges, and finally the increase of the impact force of the second wedge compared to the first wedge in terms of percentage of the first wedge maximum impact force.

4.1. Deadrise = 30 and d/W = 1

The evolution of free surface for different heel angles is illustrated in Fig. 10 for 30 degrees deadrise and d/W = 1.

As observed in Fig. 10, the spray formation of the second wedge (the right wedge) is increasingly affected by the first as the heel angle increases. This trend of influence is also observed in the impact force of the right wedge in Fig. 11.

It is quite clear that the first wedge (the left wedge) has significant effect on the right wedge impact forces and as the heel angle increases, this effect increases. It is also observed that the impact time of the occurrence is affected and impact duration is diminished for the higher heel angles. The diminishment of the impact duration of the second wedge may be due to the entrapment of its inner part spray. As deduced by the evolution of the free surfaces, the spray formed by the first wedge entraps the spray of the second wedge, increasing its pressure and decreasing its time of evolution. This implies that the impact force of the second wedge is larger and more instantaneous than that of the first wedge. For a better view of the maximum impact force trend for both wedges, the maximum impact force versus heel angle and the times of occurrence of the maximum force are illustrated in Fig. 12.

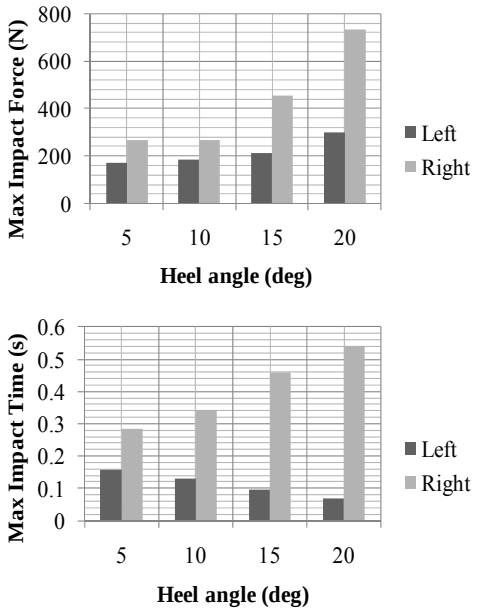

Fig. 12. Maximum impact force and time of the occurrence Vs heel angles for the left and right wedges, deadrise = 30 deg., d/W = 1.

As evident in Fig. 12, the time of occurrence of the impact is increasing with heel angle for the right wedge, while it is decreasing for the left wedge. This is due to the fact that higher heel angles imply that second wedge is farther from the free surface which delays the impact of the second wedge. However, the first wedge acts like a wedge with lower deadrise, which has relatively higher impact force than the higher deadrise and faster occurrence.

It is also observed again in Fig. 12 that the presence of the left wedge critically affects the right wedge, highly increasing its impact force. The percentage of the impact force increase is illustrated Fig. 13.

As shown in Fig. 13, the impact force of the right (second) wedge is increased by 40% up to 144% of the left (first) wedge which is a very significant increase. It is also observed that this effect generally increases with a local decrease for the 10 degrees heel angle. The reason for this decrease may be found in the evolution of the impact force. It is observed that the impact force of the 10 degrees deadrise is broken in two parts which significantly decreases the impact maximum force.

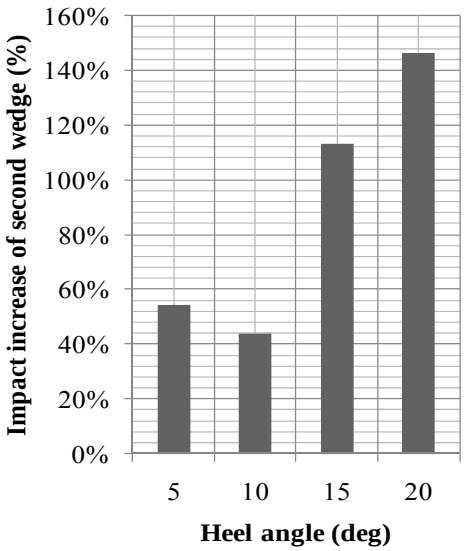

Fig. 13. Percentages of the increase of second wedge maximum impact force Vs heel angles, deadrise = 30 deg., d/W = 1.

4.2. Deadrise = 30 and d/W = 2

In this section, similar to the case of 30 degrees deadrise and d/W = 1, the results are presented for the deadrise 30 and d/W = 2. As the wedges are farther from each other, a decrease in the effects of the first wedge is expected.

As seen in Fig. 14, because of the distance between the wedges, the reciprocal effects on free surfaces and spray evolution are diminished. This is also observed in the impact force evolution in Fig. 15.

As observed in Fig. 15, no significant change is induced for the first wedge forces by increasing the wedge separatin (d/W). However, the behavior of the second wedge has significantly changed. The impact forces are diminished and obviously the

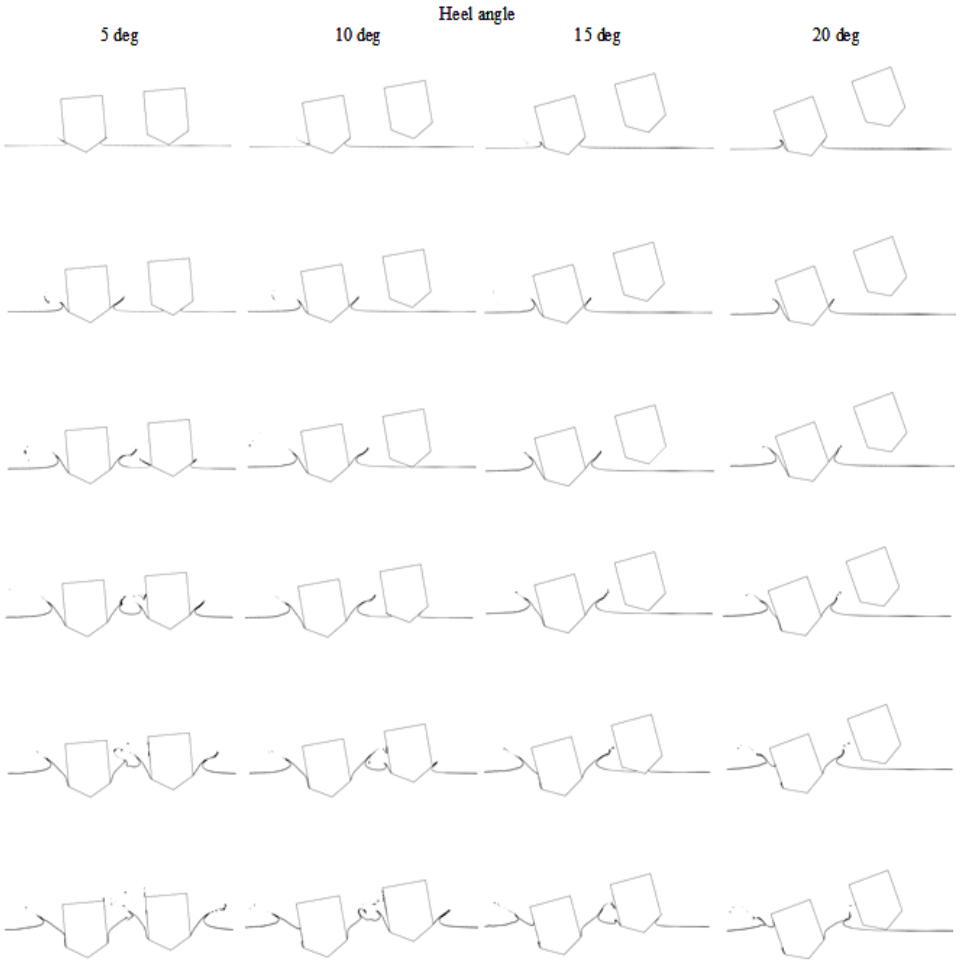

Fig. 14. Free surface evolution at different heel angles, deadrise = 30 deg., d/W = 2.

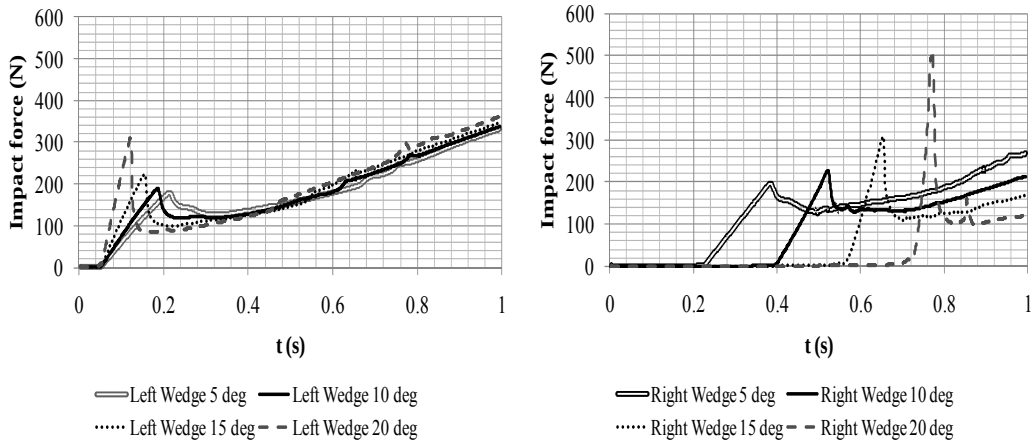

Fig. 15. Impact force Vs time at different heel angles for the left and right wedges, deadrise = 30 deg., d/W = 2.

impact occurrence time increases. This is better shown in the charts of Fig. 16.

On the other hand, the percentage of impact force increase is illustrated in Fig. 17. It is observed in Fig. 17 that the impact force of the right wedge is still affected by the first wedge, but this time up to 60%. As logically expected, by increasing the wedges separation infinitely, this effect would decrease to 0%.

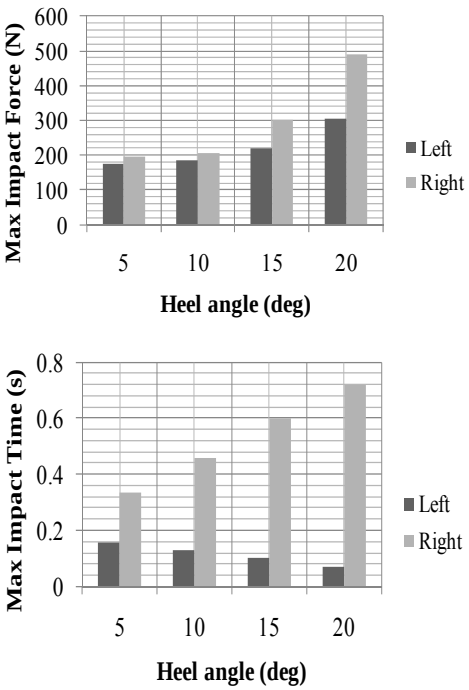

Fig. 16. Maximum impact force and time of occurrence Vs heel angles for left and right wedges, deadrise = 30 deg, d/W = 2.

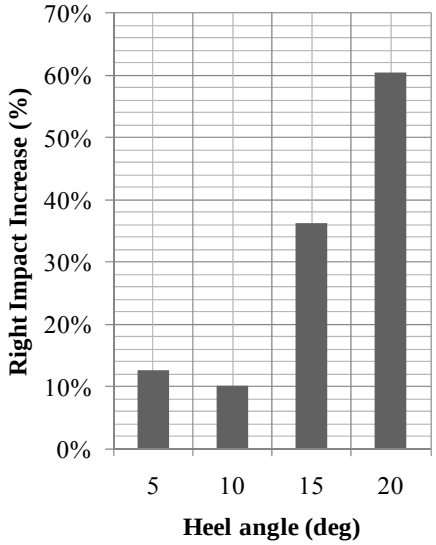

Fig. 17. Percentage of the increase in second wedge maximum impact force vs. heel angles, deadrise = 30 deg., d/W = 2.

4.3. Deadrise = 50 and d/W = 1

After discussing the 30 degrees deadrise, the same analysis and discussion is presented for 50 degrees deadrise and d/W = 1 and 2 in the present and following sections. It should be pointed out that because of the increase in deadrise, a decrease in impact forces and sprays are anticipated. Consequently, a global decrease in the effects of the first wedge on the second is expected.

As expected, the free surface perturbations are much smaller than in the case of 30 degrees deadrise angle, as shown in Fig. 18.

As evident in Fig. 19, the forces are smaller than that of 30 degrees deadrise and it is also observed that the effect of the first wedge on the second is smaller than that of 30 degrees wedge. However, there are still significant effects which can be better observed in Figs. 20 and 21.

As mentioned before, the effects of the first wedge on the second wedge maximum impact force are still significant and range from 35% to 114%.

4.4. Deadrise = 50 and d/W = 2

Similar to the case of 30 degrees deadrise, the increase in d/W is expected to affect the reciprocal effects of the wedges. In this section, the water entry is analyzed for the 50 deadrise angle and d/W = 2.

As expected, the effects of the left wedge on the right wedge are decreased because of the increase in

the distance between two wedges, as displayed in Fig. 22.

Also, as observed in the force plots of Fig. 23, although the impact forces of the second wedge increase, but this time, the increase is significantly decreased. This can better be observed in Fig. 24.

As observed in Fig. 25, the effect of the first wedge on the second is limited to a maximum of 29% for the 20 degrees heel angle.

4.5. Comparative Discussion

After presenting the results for different deadrises at different wedge separations and different heel angles, a comparative discussion is presented here on the maximum impact forces of different cases on the first and second wedges.

Firstly, as observed in the figures presented in the last section, the effects of the second wedge on the first wedge are limited to a significant time after the impact of the first wedge. Therefore, it is expected that the first wedge impact is not affected by the second wedge. This expectation can be verified in Fig. 26 where the maximum impact forces of the first wedge are presented simultaneously for different cases.

As observed in Fig. 26, the maximum impact force of the first wedge is solely affected by the wedge deadrise and heel. The effects of d/W are negligible which show the negligible effects of the second wedge on the first wedge impact. This is not the case for the second wedge which can be assessed using Fig. 27.

As evident in Fig. 27, the impact force of the second wedge is significantly affected by the first wedge in a range of 6% to 146%. The effects are highly dependent on the heel angle. It should also be mentioned that the variation of efficacy of the first wedge on the second is not monotonic versus heel angle or deadrise.

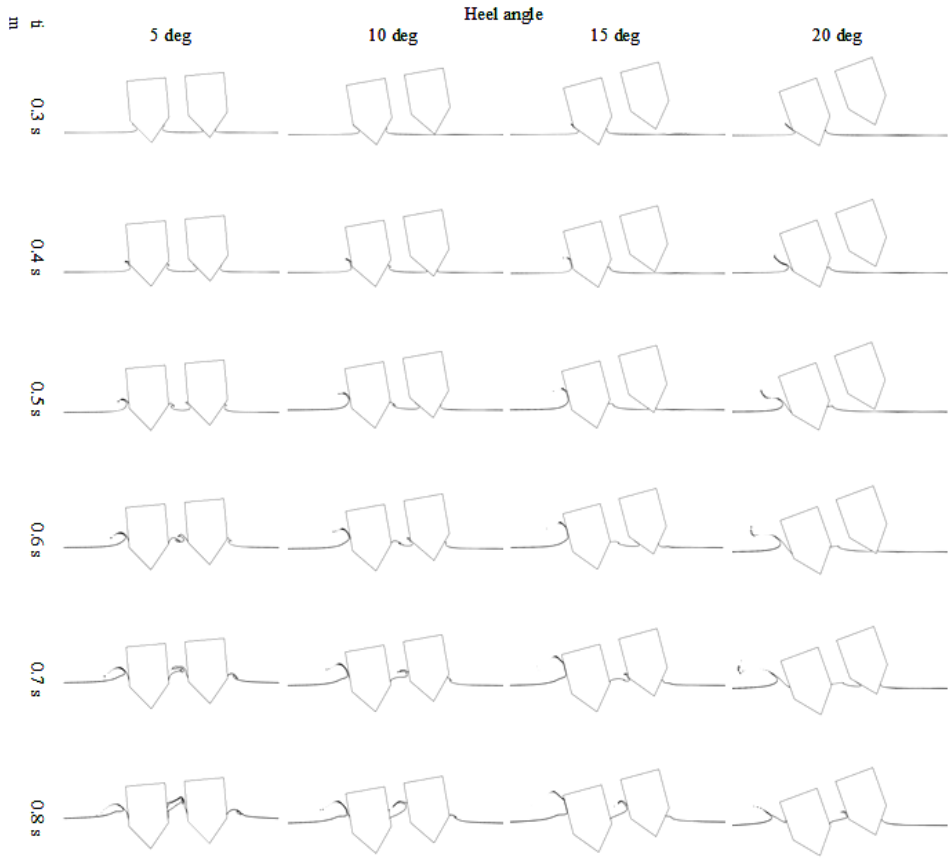

Fig. 18. Free surface evolution at different heel angles, deadrise = 50 deg, d/W = 1.

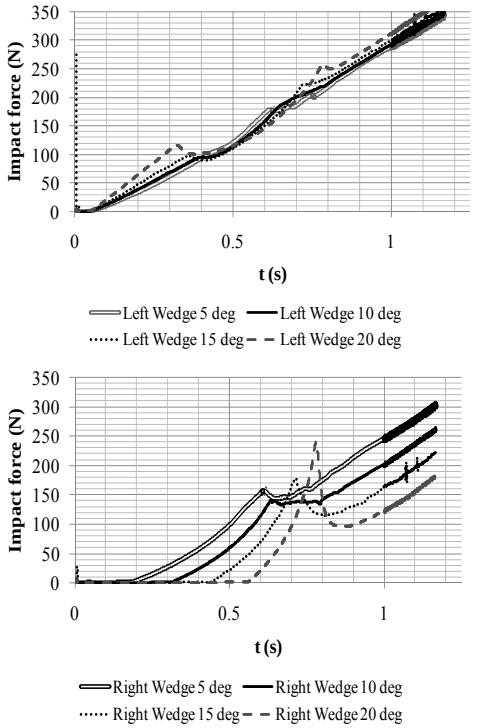

Fig. 19. Impact force Vs time at different heel angles for left and right wedges, deadrise = 50 deg., d/W= 1.

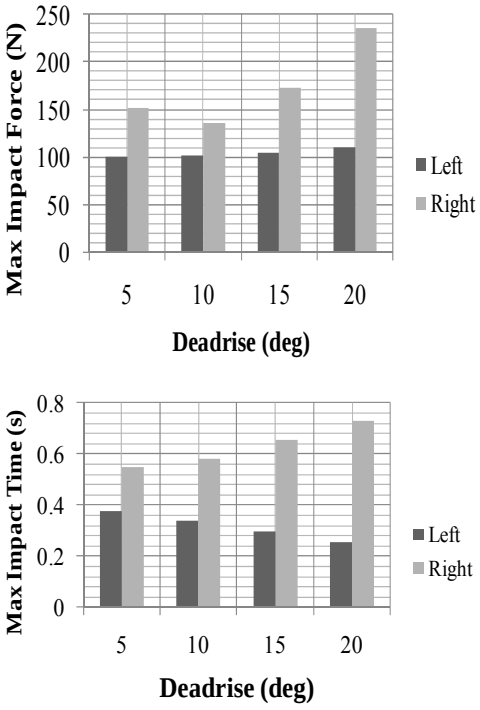

Fig. 20. Maximum impact force and time of the occurrence Vs heel angles for left and right wedges, deadrise = 50 deg., d/W = 1.

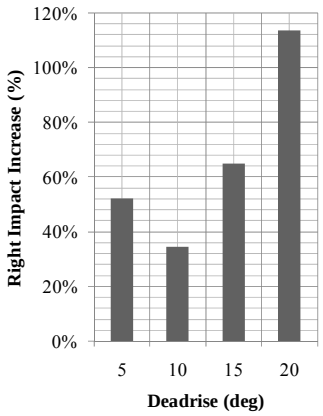

Fig. 21. Percentage of increase of the second wedge maximum impact force Vs heel angles, deadrise = 50 deg., d/W = 1.

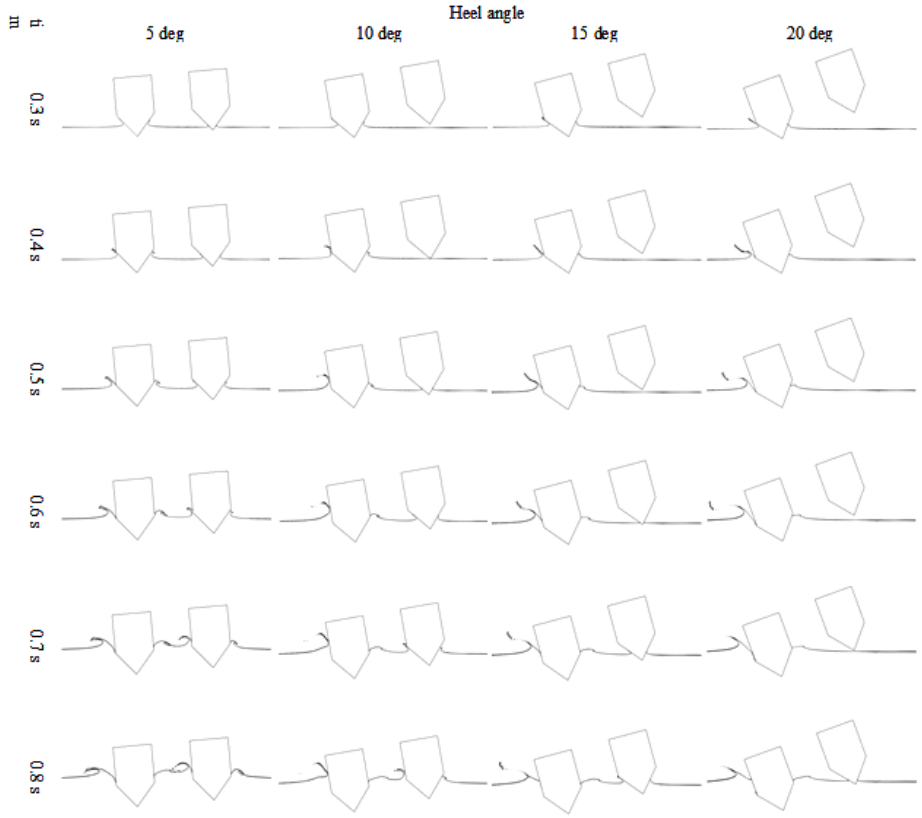

Fig. 22. Free surface evolution at different heel angles, deadrise = 50 deg, d/W = 2.

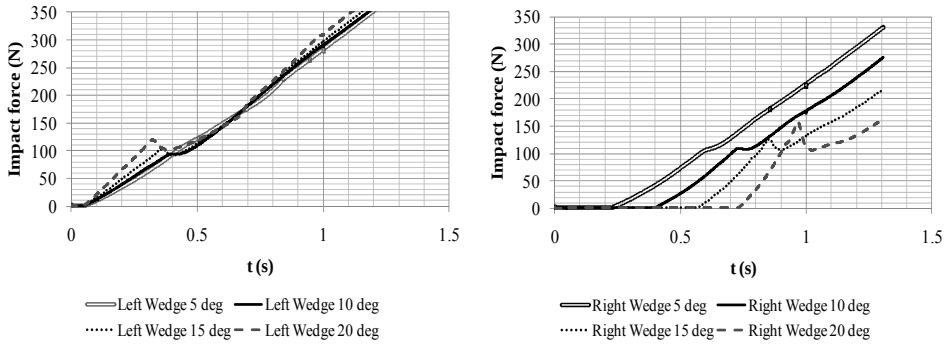

Fig. 23. Impact force Vs time at different heel angles for the left and right wedges, deadrise = 50 deg., d/W = 2.

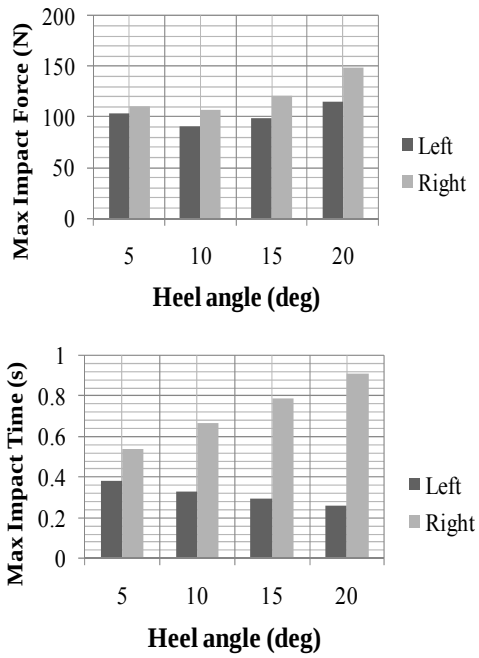

Fig. 24. Maximum impact force and the time of occurrence Vs heel angles for left and right wedges, deadrise = 50 deg., d/W = 2.

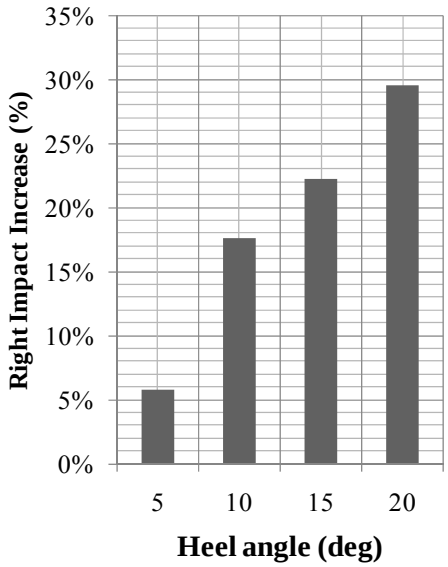

Fig. 25. Percentage of the increase of second wedge maximum impact force Vs heel angles, deadrise = 50 deg., d/W = 2.

5. CONCLUSION

Water entry of twin wedges can be used in hydrodynamic and structural analysis of planing catamarans. The present study focuses on the asymmetric water entry of twin wedges, which represents the heeled state of a catamaran hull for 4 different heel angles (5, 10, 15, and 20 degrees), 2 deadrises (30 and 50 degrees) and 2 wedge separations (d/W = 1 and 2). Finite Element based Finite Volume method and Volume of Fluid scheme are used for the targeted analyses which have been explained and validated throughout the paper.

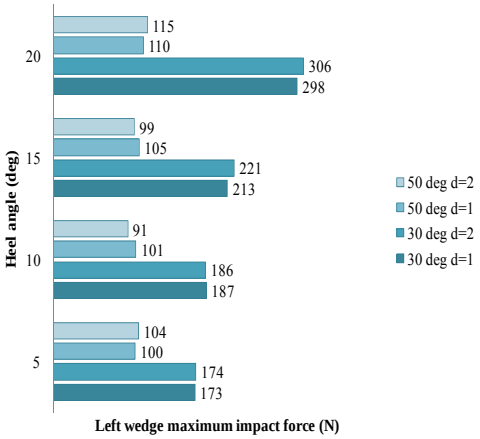

Fig. 26. Maximum impact forces of the first wedge for different cases.

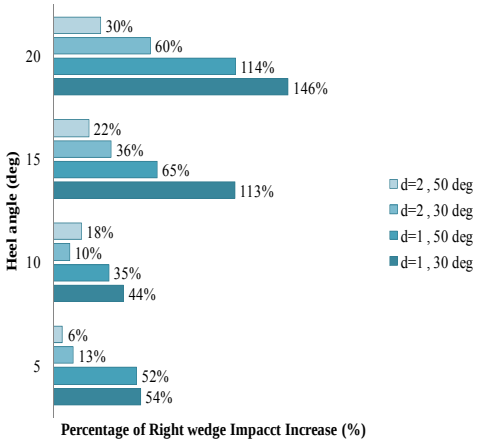

Fig. 27. Percentage of the impact forces increase in the second wedge for different cases.

The results of the analyses have been presented in the forms of the free surface evolution and the impact forces versus time separately for the wedges, and comparison of the maximum impact force of the two wedges. It has been demonstrated that during the water entry, the maximum impact force of the first wedge entering the water is not significantly affected by the second one. However, the free surface formation and the impact forces of the second wedge are dramatically influenced by the first wedge. It has been observed that the impact force on the second wedge is always greater than the first wedge by a minimum of 6% for 5 degrees heel and d/W = 2 and up to 146% for 20 degrees heel and d/W = 1. This is a very significant increase in the impact force which can cause high

accelerations and structural damages on catamarans and should be considered in the design process of the catamaran planing hulls. It has also been illustrated that the effects of the first wedge on the second is increased by increasing the heel angle and also by decreasing the deadrise angle.

REFERENCES

Battistin, D. and A. Iafrati (2004). A numerical model for the jet generation by water impact. *J Eng. Math* 48, 353-374.

Faltinsen, O. M. (2002). Water entry of a wedge with finite deadrise angle. *J Ship Res* 46(1), 39-51.

Faltinsen, O. M., M. Landrini and M. Greco (2004). Slamming in marine applications. *J Eng Math* 48(3-4), 187–217.

Farsi, M. and P. Ghadimi (2015). Simulation of 2D symmetry and asymmetry wedge water entry by smoothed particle hydrodynamics method. *J Braz. Soc. Mech. Sci. Eng*. 37(3), 821-835.

Farsi, M. and P. Ghadimi (2016). Effect of flat deck on catamaran water entry through smoothed particle hydrodynamics. In *Proceedings of the Institution of Mechanical Engineers, Part M: Journal of Engineering for the Maritime Environment* 230(2) 267-280.

Farsi, M., P. Ghadimi, R. Zamanian and A. Dashtimanesh (2013). Numerical Simulation of wedge water entry using smoothed particle hydrodynamics method. *Int. J. Sci. World* 1(1), 5-12.

Gao, J., Y. Wang and K. Chen (2011). Numerical simulation of the water entry of a wedge based on the complex variable boundary element method. *App. Mech. and Mater.* 90-93, 2507-2510.

Ghadimi, P., A. Dashtimanesh, S. R. Djeddi (2012). Study of water entry of circular cylinder by using analytical and numerical solutions. *J Brazilian Society of Mech Sci Eng.* 37(3), 821-835.

Ghadimi, P., A. Saadatkhah and A. Dashtimanesh (2011). Analytical solution of wedge water entry by using Schwartz-Christoffel conformal mapping. *Int. J. Model. Sim. Sci. Compu.* 2(3), 337-354.

Ghadimi, P., M. A. Feizi Chekab and A. Dashtimanesh (2013). A Numerical investigation of the water impact of an arbitrary bow section. *ISH Journal of Hydraulic Engineering* 19(3), *186-195.*

Ghadimi, P., M. A. Feizi Chekab and A. Dashtimanesh (2014). Numerical simulation of water entry of different arbitrary bow sections. *J. Naval Arch. Marine Eng.* 11, 117-129.

Ghadimi, P., S. Tavakoli, and A. Dashtimanesh (2015). An analytical time procedure for time domain simuation of roll motion of the warped planing hulls. *J. Eng. Maritime Envion*.

Greenhow, M. (1988). Water-entry and -exit of a horizontal circular cylinder. *App. Ocean Res.* 10, 191–198.

He, W., T. Castiglione, M. Kandasamy and F. Stern (2011). URANS Simulation of Catamaran Interference. In *proceeding of 11th International Conference on Fast Sea Transportation, FAST,* Honolulu, Hawaii, USA.

Karimian, S. M. H., G. E. Schneider (1994). Pressure-based computational method for compressible and incompressible flows. *J. Thermo Physics and heat Transfer* 8(2), 267-274.

Khabakhpasheva, T. and A. Korobkin (2012). Elastic wedge impact onto a liquid surface: Wagner's solution and approximate models. *J. of Fluids and Structures* 36, 32-49.

Luo, H., H. Wang and C. G Soares (2011). Numerical prediction of slamming loads on a rigid wedge subjected to water entry using an explicit finite element method. *Advances in Marine Structures* – In *Proceedings of the 3rd International Conference on Marine Structures.*

Luo, H., H. Wang and C. G. Soares (2012). Numerical and experimental study of hydrodynamic impact and elastic response of one free-drop wedge with stiffened panels. *Ocean Eng.* 40, 1-14.

Mo, L., H. Wang, C. Jiang and C. Xu (2011). Study on dropping test of wedge grillages with various types of stiffeness. *Journal of Ship Mechanics* 4, 394-40.

Mutsuda, H. and Y. Doi (2009). Numerical simulation of dynamic response of structure caused by wave impact pressure using an Eulerian scheme with Lagrangian particles. In *Proceedings of the International Conference on Offshore Mechanics and Arctic Engineering - OMAE.*

Panciroli, R. (2013). Water entry of flexible wedges: Some issues on the FSI phenomena. *App. Ocean Res.* 39, 72-74.

Panciroli, R., S. Abrate, G. Minak and A. Zucchelli (2012). Hydroelasticity in water-entry problems: Comparison between experimental and SPH results. *Composite Structures* 94(2), 532-539.

Piro, D. J. and K. Maki (2013). Hydroelastic analysis of bodies that enter and exit water. *J. Fluids and Structures* 37, 134-150.

Rhie, C. M., W. L. Chow (1983). Numerical study of the turbulent flow past an airfoil with trailing edge separation. *AIAA Journal* 21(11), 1525-1532.

Shademani, R., P. Ghadimi (2016). Estimation of water entry forces, spray parameters and secondary impact of fixed width wedges at extreme angles using finite element based finite volume and volume of fluid methods. *J Brodogradnja* 67(2), 101-124.

Shah, S. A., A. C. Orifici and J. H. Watmuff (2015). Water impact of rigid wedges in two-dimensional fluid flow. *Journal of Applied Fluid Mechanics* 8(2), 329-338.

Sun, H., J. Zou, J. Zhuang and Q. Wang (2011). The computation of water entry problem of prismatic planning vessels. In *3rd International Workshop on Intelligent Systems and Applications.*

Tveitnes, T., C. A. Fairlie-Clarke and K. Varyani (2008). An experimental investigation into the constant velocity water entry of wedge-shaped sections. *Ocean Eng.* 35, 1463–1478.

Von Karman, T. (1929). The impact of seaplane floats during landing. *NACA TN 321*. Washington, DC.

Wagner, H. (1932). The phenomena of impact and planing on water. *National Advisory Committee for Aeronautics, Translation, 1366*, *Washington, DC ZAMM. J. App. Math. Mech.* 12(4), 193–215.

Wang, Y. H. and Z. Y. Wei (2012). Numerical analysis for water entry of wedges based on a complex variable boundary element method. *Explosion and Shock Waves* 32(1), 55-60.

Wu, G. (2012). Numerical simulation for water entry of a wedge at varying speed by a high order boundary element method. *J. Marine Sc. App*. 11(2), 43-149.

Yamada, Y., T. Takami and M. Oka (2012). Numerical study on the slamming impact of wedge shaped obstacles considering fluid-structure interaction (FSI). In *Proceedings of the International Offshore and Polar Engineering Conference.*

Yang, Q. and W. Qiu (2012). Numerical Solution of 3-D Water Entry Problems with a Constrained Interpolation Profile Method. *J. Offshore Mech. Arctic Eng.* 134(4).

Yousefnezhad, R and H. Zeraatgar (2014). A parametric study on water-entry of a twin wedge by boundary element method. *J Mar Sci Technol* 19, 314-326.

Zhao, R. and O. M. Faltinsen (1993). Water entry of two-dimensional bodies. *J Fluid Mech*. 246, 593-612.

Zhao, R. and O. M. Faltinsen (1998) Water entry of arbitrary axisymmetric bodies with and without flow separation. In *proceeding of 22nd Symposium on Naval Hydrodynamics,* Washington, DC, 1998.

Zhao, R., O. M. Faltinsen and J. Aarsnes (1996). Water entry of arbitrary two dimensional sections with and without flow separation. In *1st Symposium on Naval Hydrodynamics,* Tronheim, Norway, National Academy Press, Washington, DC.

Zhu, X. Y. (2006). *Application of the CIP method to strongly nonlinear wave-body interaction problems*. Ph. D. thesis, Norwegian University of Science and Technology, Trondheim, Norway.